

June 27-28, 2024, İstanbul, Türkiye

4th Maritime Security Conference

https://www.marseccoe.org/

New electromagnetic technology for the detection of underwater objects: Principle and results of tests carried out at NATO - CMRE

Lyes Ifrek ¹, Graham Pulford ¹, Pierre Aubry ¹, Per Arne Sletner ²

¹Research & Development, ELWAVE, Carquefou, France ²Sonar and Marine Sensors Section, NATO-CMRE, La Spezia, Italy

lyes.ifrek@elwave.fr

I. ABSTRACT

This paper presents a new technology, CEDAR (Controlled Electric Detection And Ranging) developed by Elwave and integrated into its Octopulse product line that enables the detection of underwater objects exhibiting a contrast in electrical conductivity compared with that of the seawater and sediment background. This technology is based on the emission of an electrical alternating current through an active emitting dipole along with the measurement of the variations of two electrical impedances: an explicit impedance within the emitting dipole and an apparent impedance measured by passive receiver dipoles. Dipoles can be emitters or receivers and, by using multiple dipoles, measurements may be made in different polarization directions in the environment. Tests of the Octopulse system were carried out at the NATO CMRE UXO Testbed in La Spezia, Italy. After describing the underlying principles of "electric sense" incorporated in the product, we first detail the system architecture and its signal processing applied to the amplitude and phase of the measured impedances. This is followed by a description of the sea trials and an analysis of the results obtained, which clearly demonstrate an effective capability to detect targets present in the test area.

II. INTRODUCTION

Detection and characterization of unexploded ordnance (UXO) using modern electromagnetic sensors is widespread on land [Gas06], [Bar06]. However, it is estimated that up to one million acres of underwater sites

may also be contaminated with hazardous UXO [MCD06] and different methods must be applied for underwater UXO detection. Elwave's new system is based on bio-inspired electric sense.

Sea trials have recently been carried out by Elwave in the CMRE UXO Testbed at La Sepezia. The Testbed consists of an underwater area containing various unexploded ordnance and artificial clutter objects of different shapes and dimensions deployed at known positions on the seabed.

The electric sense was discovered by Lissman in 1958 when studying sensory perception of weakly electric fish [LM58]. This sense has evolved in hundreds of fish species across Africa and South America. An electric organ discharge (EOD) in the fish's tail creates a dipolar electric field. This field is distorted by surrounding objects, and the fish detects these distortions using electro-receptors along its body. Perceived signals are processed in the fish's brain to form an 3D image of its environment [CBG+98].

Electric fish can navigate effortlessly in dark or murky waters. Unlike visual imaging or sonar, which may fail in such conditions, the electric sense is better suited for these environments. Building on this capability [SLM07] conducted experiments using four-point electrodes arranged in a rhombus on a rigid moving frame to explore this phenomenon further.

Several concepts for underwater operations have been explored by Elwave and IMT Atlantique using the electric sense. In [ELW20] a bio-inspired electric sensor

was integrated onto a ROV to detect and avoid obstacles for navigation in turbid water.

One of the key strengths of the Elwave Octopulse sensor is the versatility of its electrode array, which can operate simultaneously in both active and passive modes. This flexibility allows the environment to be polarized in multiple orientations. The ability to simultaneously measure via an active dipole oriented in one direction with passive dipoles oriented in other directions enables the capture of an instantaneous electrical image. A 2D map of the seabed is built from the processed electrical data showing both the conductive objects (ferromagnetic or non-magnetic) and the insulators. Additionally, Octopulse is compatible with various vehicle shapes and sizes, including ROVs, AUVs, USVs, and ROTVs. In particular, for autonomous vehicles, Octopulse is an ideal candidate for UXO detection in low visibility situations because of its low power consumption.

The rest of the paper is structured as follows. Section III presents the relevant electromagnetic theory for the electric sense, leading to the design of the Octopulse sensor in section IIIB. Section IIIC deals with the impedance signal processing for dipole measurements. Section IV concerns the plan for the sea trials. Section V presents the detection results for different targets. Section VI highlights important parameters affecting the results. Conclusions are drawn in section VI.

FROM THEORY TO ENGINEERING III.

A. Electric sense theory

An electrical power source is equivalent to a dipole with symmetric lobes of positive and negative potential. The potential distribution $\phi(r, \alpha)$ of an ideal dipole at a distance r and angle α from the body axis in a homogeneous water medium is given by the formula:

$$\phi(r,\alpha) = \frac{I(t)}{4\pi\sigma_w} \frac{\cos{(\alpha)}}{r^2}$$

where σ_w is the water conductivity and I(t) the electrical current of the source, which is generally time varying.

At each point in space \vec{r} , the electric field \vec{E} is defined by the gradient of the potential:

$$\vec{E}(\vec{r}) = -\nabla \phi(\vec{r})$$

The electric field induces an electric current density distribution according to Ohm's law:

$$\vec{J} = \sigma_w \vec{E}$$

For modelling the nominal electric field in the water medium generated by the power source due to the presence of an object, the simplest case is a spherical object, which gives an analytical response. Other geometries must in general be modelled with finite element or other numerical methods.

The presence of a sphere in the electric field generated by the source results in an additional dipole field superimposed to the original field. For each frequency ω , the amplitude of the potential of this induced dipole is determined, indicating how the sphere modifies the overall electric field by adding a frequency-dependent dipole component [RAS 96]:

$$\phi_s(\vec{r},\omega) = \chi(\omega) \cdot R^3 \cdot \vec{E}(\vec{r}_s,\omega) \cdot \frac{(\vec{r} - \vec{r}_s)}{|\vec{r} - \vec{r}_s|^3}$$

where R is the radius of the sphere, $\vec{E}(\vec{r}_s, \omega)$ is the source field phasor (complex amplitude and phase) at frequency $\omega = 2\pi f$, and $\chi(\omega)$ the electrical contrast defined as:

$$\chi(\omega) = \frac{\sigma_s - \sigma_w + i\omega(\varepsilon_s - \varepsilon_w)}{\sigma_s + 2\sigma_w + i\omega(\varepsilon_s + 2\varepsilon_w)}$$
 where σ_s , σ_w and ε_s , ε_w are the conductivities and

permittivities of the sphere and water respectively.

B. Bio-inspired sensor design

In the early design stage of the development of the Octopulse sensor, research was conducted by Elwave's academic partner IMT Atlantique in Nantes. One of the first bio-inspired electric sensors utilised an elongated cylindrical probe, as described in [LBLB17]. It was composed of eight metal electrodes housed in an insulting cylinder body. Each electrode was driven by a 22 kHz AC signal generator to generate a primary electric field. This sensor probe was used to firstly detect and characterize an object material, secondly to localize the object and finally to estimate the shape of the object.

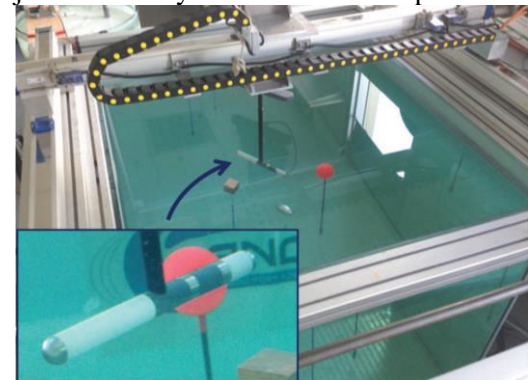


Figure 1: Cartesian robot moving the elongated probe near conductive and insulating objects in test tank ([LBLB17] with permission from IMT Atlantique).

The sensor was subsequently matured to a high technology readiness level suitable for industrial applicability:

- Pod containing the electronics card upgraded to resist a pressure of 37 bars (~300 m depth).
- Sensor sensitivity increased to measure weaker signals.
- Maximum source power increased to 24 volts at 2
- The frequency range was extended to 100Hz to 30kHz to cater for different applications in terms of

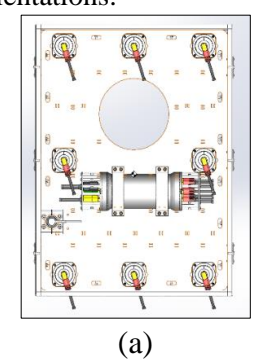
- survey depth, vehicle altitude, water conductivity and target dimension.
- Measurement of two impedances: an explicit impedance measured at the power source, and an apparent impedance measured between remaining electrodes.

The sensor is compatible with a large number of vehicle shapes (ROV, AUV, USV, ROTV ...).



Figure 2: Octopulse POD with 8 electrodes.

For use with ROVs the eight electrodes are placed on an insulating "skid" mounted below the ROV. Electrodes are numbered from 1 to 8 as in Figure 3 (b) and oriented toward the sea floor to scan the field streamlines and penetrate the sediment. Generally, two electrodes are used to form the dipolar power source with the six remaining electrodes measuring a spatially distributed potential. The power source is switched from one dipole to another one in order to polarize the object at different orientations.



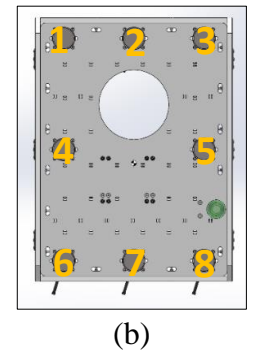


Figure 3: ROV skid containing Octopulse POD with 8 electrodes: (a) top view, (b) bottom view.

Figure 4 shows the finite element modelling of a dipolar source in seawater in the presence of an object. The streamlines are attracted by a conductor (Figure 4 (a)) and repelled by an insulator (Figure 4 (b)).

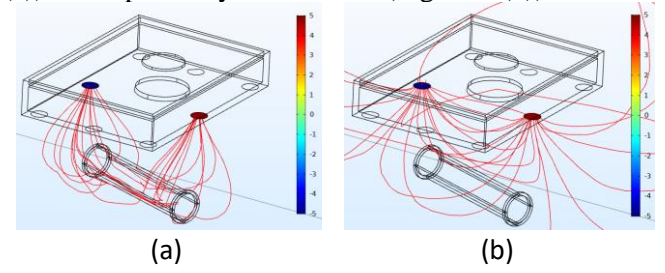


Figure 4 : COMSOL electromagnetic simulation, dipolar voltage source and electrical current streamlines, (a): conductive target, (b): insulating target.

Figure 5 (a) shows the electric potential on the electrode surface of the $\pm 5V$ power source versus the electric potential on the remaining electrodes in the presence of an insulating object ($\pm 0.1V$) in Figure 5 (b)

Two impedances are calculated: Z_e an explicit impedance which is the ratio between the source voltage V_s and the source current I_s ; Z_a an apparent impedance which is the ratio between the measured voltage V_a at different points and the source current I_s :

$$Z_e = \frac{V_s}{I_s} \qquad Z_a = \frac{V_a}{I_s}$$

In the remainder of the paper, we adopt the terminology "active dipole" (subscript A) for the explicit impedance, and "passive dipole" (subscript P) for the apparent impedance.

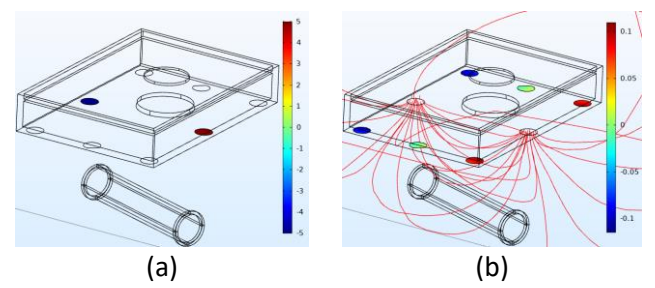


Figure 5: COMSOL electromagnetic simulation with 8-electrode sensor: (a) electric potential on two electrodes forming a dipolar source; (b) electric potential on remaining 4 electrodes.

C. Signal Processing

Figure 6 depicts the electrical measurements for an active dipole (electrodes 1 and 2) and a passive dipole (electrodes 3 and 4). The signal source is a pure AC sinewave with frequency f_0 applied on the active dipole, inducing a current I_A and voltage V_A in the seawater medium. A corresponding potential V_P is measured on the passive dipole.

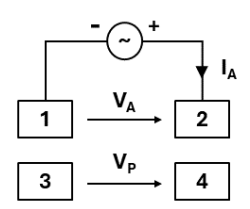


Figure 6: AC Measurements with active and passive dipoles.

A block diagram of the generic receiver signal processing is shown in Figure 7. Following analogue to digital conversion, the noisy voltage and current samples are transformed by a DFT applied at the carrier frequency f₀. This is followed by arithmetic averaging of the real (Re) and imaginary (Im) parts of the complex DFT coefficients. The complex impedance is obtained as

$$Z = \frac{V_{Re}(f_0) + jV_{Im}(f_0)}{I_{Re}(f_0) + jI_{Im}(f_0)}$$

$$V \longrightarrow DFT(f_0) \xrightarrow{Re} Average \longrightarrow V_{Re}(f_0)$$

$$I \longrightarrow DFT(f_0) \xrightarrow{Re} Average \longrightarrow I_{Re}(f_0)$$

$$I \longrightarrow DFT(f_0) \xrightarrow{Im} Average \longrightarrow I_{Im}(f_0)$$

Figure 7: Generic receiver signal processing.

The data processing is applied separately to the amplitude and phase channels of the complex impedance measurements. The processing of the impedance magnitude is shown in Figure 8, with similar processing applying to the phase of the impedance. The first stage of the data processing is a conventional outlier rejection filter based on the well-known Hampel algorithm. This is followed by normalisation processing to obtain a workable numerical range for the display and to facilitate target detection at the operator level. Positioning data in latitude (λ) and longitude (ϕ) are provided by the navigation system on the ROV. The navigation and impedance data streams are synchronized construction of a 2D impedance map that is displayed using QGIS software. This is currently performed as post-processing.

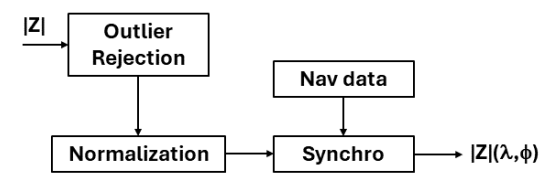


Figure 8: Impedance processing with inclusion of 2D position data.

IV. TEST PLAN

The mission was conducted in collaboration with CMRE. Argos ROV from Forssea Robotics was used for its compact size and manoeuvrability. The ROV is 1.1 m in length and 0.79 m in width. It was equipped with an Octopulse sensor mounted on an adapted skid (see FIGURE 9). For positioning, the Argos ROV was combined with a suite of iXblue USBL sensors: a ROVINS nano, a MT9 Beacon, and a GAPS acoustic positioning system. This combination of sensors gives an approximate positioning error standard deviation of 30 cm near the survey vessel. Overall positioning error for the sea trial was around 1 metre.

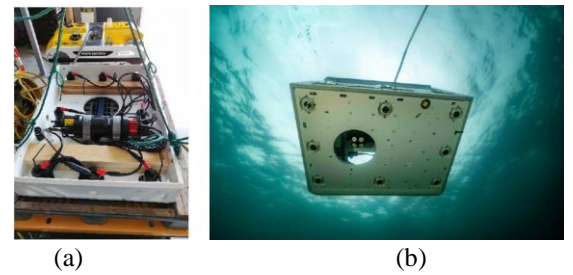


Figure 9: Octopulse sensor mounted on Argos ROV

The CMRE testbed spans about 1 km² (540 m x 220 m) with an average water depth of 10 metres ranging from 5 to 12 metres. The seabed is composed of homogeneous mud and sand sediment. The test was conducted on the calibration area containing twelve targets distributed along a line with a spacing of approximately 15 meters (see Figure 10).

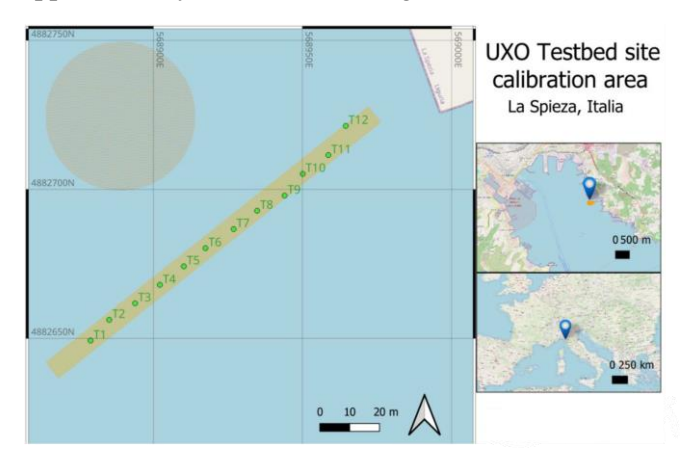


Figure 10 : Calibration area location with twelve targets (T1 to T12)

The targets are of different dimensions and materials (conductive and insulating, see Table 1). Note that since targets T1 and T12 are identical, to save time during the tests, we measure only T1.

N°	Picture	Size	Material
T1	Calibration area Target	tied to 40 kg	hard
		iron block	plastic
			and steel
			ballast
T2	Fire extinguisher	L=491mm	steel-
	WINDSPECTATION	D=161mm	sheets,
	71		rubber
T3	155mm artillery projectile	L=680mm	steel
		D=163 mm	
T4	M53 mortar projectile	L=282 mm	steel,
		D=80mm	aluminiu
			m
T5	Cement block	LxWxH:492x	cement,
		195x195	isolating

T6	70mm/127mm projectile	L=700mm	steel
		D=70mm	
T7	40mm projectile	L=212 mm	steel,
		D=41mm	aluminiu m
Т8	127mm navy projectile	L=640mm	steel
		D=126 mm	
Т9	76mm naval projectile	L=354mm	steel
		D=80mm	
T10	Anchor	11160 g	steel, zinc
	6		treated
T11	105mm artillery projectile	L=473 mm	steel
		D=106mm	
T12	Calibration area Target	tied to 40 kg	hard
		iron block	plastic
			and steel ballast

Table 1 Target dimensions and materials

Several dipole configurations were evaluated to optimise the detection performance across the range of targets. The configurable sensor parameters that affect the detection quality are:

- Transmission frequency which affects the detection range;
- active and passive dipole lengths;
- active and passive dipole orientation versus target orientation.
- number of dipole arrangements, which influence the spatial resolution.

Based on the electrode numbering in Figure 3 (b), an example of an Octopulse sensor configuration is presented in Table 2.

Total arrangements	Frequency	Active dipole	Passive dipoles
	1kHz	45	12 - 13 - 23
		46	12 - 13 - 23
5		47	12 - 13 - 23
		57	12 - 13 - 23
		58	12 - 13 - 23

Table 2 Example of Octopulse sensor configuration.

The data were acquired with a ROV operating at an average speed of 0.3 m/s and an average altitude of 0.4 m above the sea floor while executing a raster trajectory.

The electrical impedance results for each target (T1 to T12) in Table 1 are presented in this section. In each case, two maps are plotted: amplitude and phase. A detection is declared manually by inspection of the 2D impedance maps with knowledge of the true target location. Multiple detections of each target are possible due to sequential flyovers by the ROV.

As observed in Figure 11, T1 is detected in both amplitude and phase. Since T1 target is spherical, the relative orientation of the dipole to the target does not affect the results, leading to good detection across most dipoles.

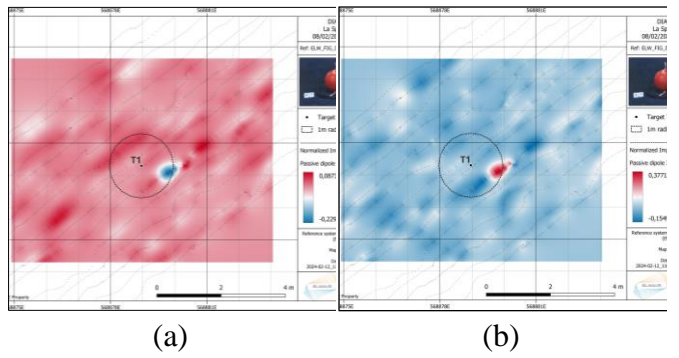


Figure 11: T1; Normalized impedance amplitude (a), phase (b)

Three configurations were tested for T2. Out of these, two successfully detected the target. There are three possible interpretations:

- Combining amplitude and phase data, T2 seems to be located 1.3 metres south of its theoretical position.
- T2 is slightly northwest of its theoretical position and was detected only in amplitude.
- T2 is at its theoretical position but was difficult to detect in amplitude due to interference from nearby objects with strong signals.

Given these possible interpretations, it was concluded that the T2 was detected but requires position confirmation from complementary sensors.

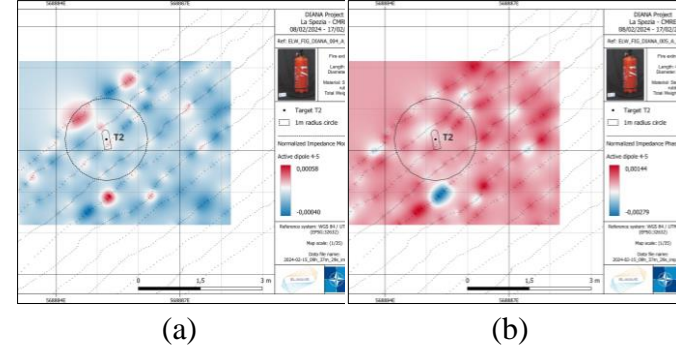


Figure 12 : T2; Normalized impedance amplitude (a), phase (b)

V. RESULTS

Among the targets T3, T4 and T5, T3 had the highest number of acquisitions, totalling 13 passes with different configurations, resulting in 11 successful detections. The strongest visible detection occurred with a configuration employing a frequency of 1 kHz and three passive dipoles. T3 was successfully detected in both amplitude and phase, as depicted in Figure 13.

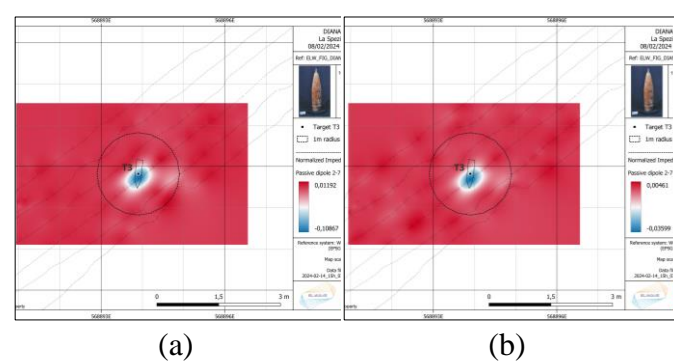


Figure 13:T3; Normalized impedance amplitude (a), phase (b)

A total of 14 configurations were tested on T4. Due to its relatively small size (282 x 80 mm), detecting this target posed a challenge. Only the configuration using active dipoles (without passive dipoles) managed to detect T4. Upon analysing both amplitude and phase data, a detection was confirmed, indicated by a hot spot located 30 cm north of the theoretical position but consistent with ROV positioning and synchronisation error, as shown in Figure 14.

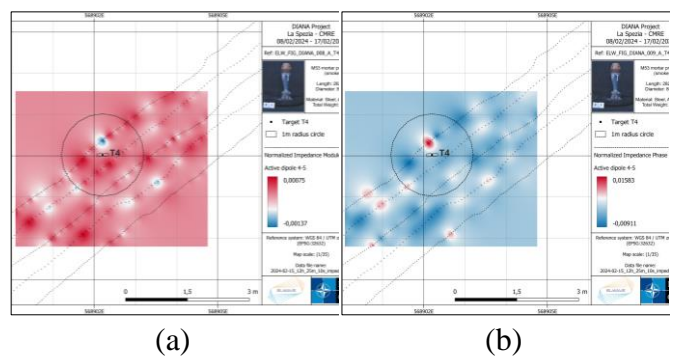


Figure 14: T4; Normalized impedance amplitude (a), phase (b)

In comparison to other targets within the calibration area, target T5 (a cement block) is characterised as an insulator (its impedance is greater than the seawater impedance). Out of 15 acquisitions, 13 successfully detected this target. As depicted in Figure 15, T5 was detected 50 cm southeast of its true position. Notably, the 2D map reveals two hot spots surrounding T5, spaced approximately at the largest dimension of T5.

Additionally, a phase detection was observed 1.5 metres north of the target, which could potentially indicate debris present in the test area.

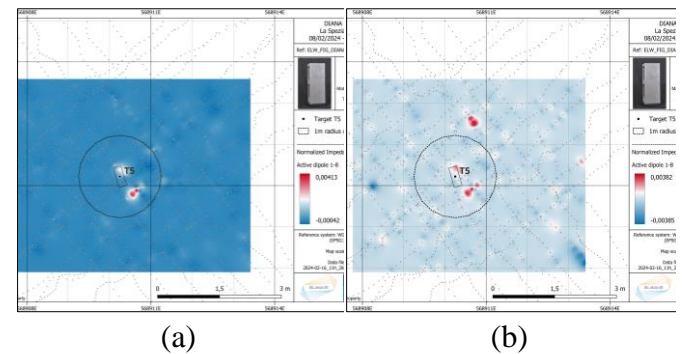


Figure 15 :T5; Normalized impedance amplitude (a) phase (b)

Regarding target T6, a total of 8 configuration were tested, with 5 of them successfully detecting the target. Figure 16 illustrates amplitude and phase detections, which appear relatively close to the theoretical target position, although the phase detection is less clear.

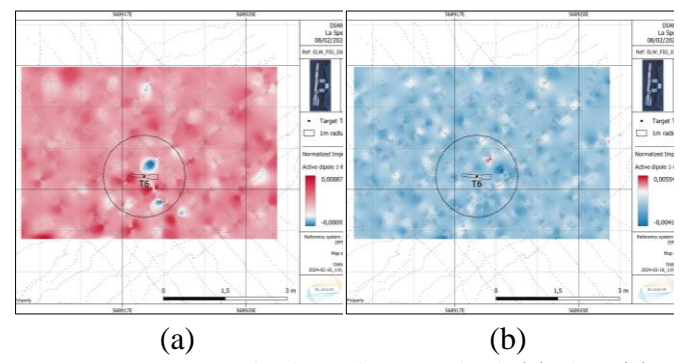


Figure 16: T6; Normalized impedance amplitude (a), phase (b)

Like T4, the small size (212 x 41 mm) of the T7 target posed a challenge for detection. The amplitude detection is situated 80 cm east of its theoretical position but is not distinctly visible due to a large positive anomaly to the south of T7. This significant anomaly is also evident in the phase data, whereas no T7 phase detection is visible.

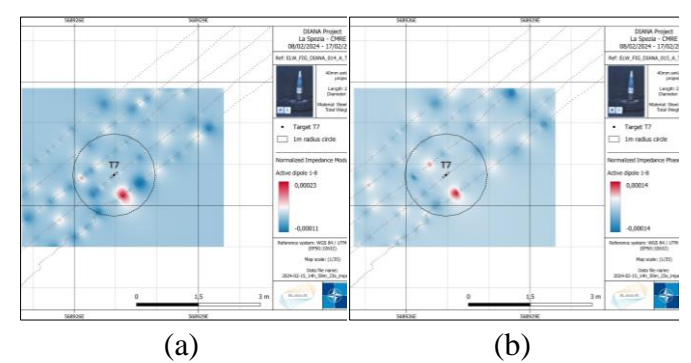


Figure 17:T7; Normalized impedance amplitude (a) phase (b)

T8 is one of the largest targets in the calibration area, along with target T3. Figure 18 displays the amplitude and phase data for passive dipole, coupled with active one. The detection is evident and closely resembles that observed on the T3 target.

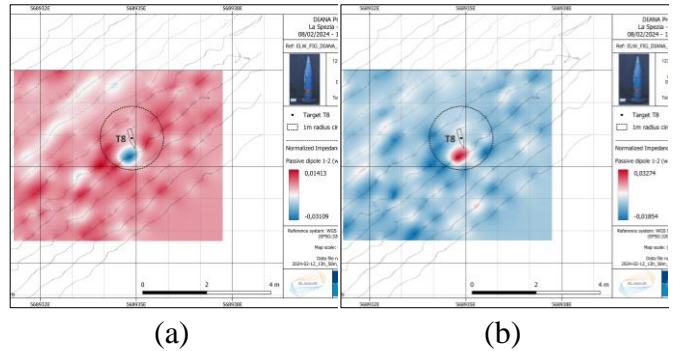


Figure 18:T8; Normalized impedance amplitude (a), phase (b)

Target T9 is one of the smallest targets in the calibration area, inherently complicating detection. Among the three configurations employed on T9, the configuration with only active dipoles yielded the most favourable detection. However, the surroundings of the T9 target appear non-uniform based on the data collected by our sensor. This is particularly evident in the phase data of Figure 19 (b). The presence of numerous anomalies around T9 restricts the detection amplitude and complicates the clear identification of T9, especially in phase.

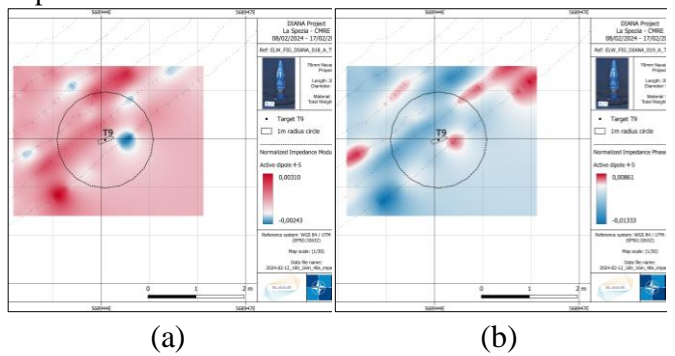


Figure 19: T9; Normalized impedance amplitude (a), phase (b)

Target T10, which is an anchor, possesses an unconventional shape compared with the other targets, resulting in a distinct electrical signature. The detection of T10 appears south of its theoretical position, displaying a double-lobed shape oriented in a north-north-west / south-south-east direction, consistent with the target's theoretical orientation of 326.1° true heading.

The phase detection of T10 is more spread out than its electrical amplitude image, presenting a pattern that is more consistent with the target's dimensions and orientation (see Figure 20).

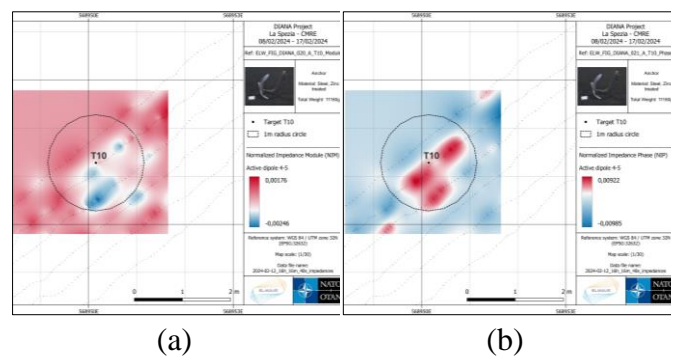


Figure 20: T10; Normalized impedance amplitude (a), phase (b)

T11 exhibited its clearest detection using the same configuration as that used for T9 and T10. T11 has a comparable detection signature to T3 and T8. However, unlike the latter, the environment surrounding T11 appears less homogeneous. Notably, two amplitude anomaly and one phase anomaly are distinguishable to the north of T11's theoretical position (see Figure 21).

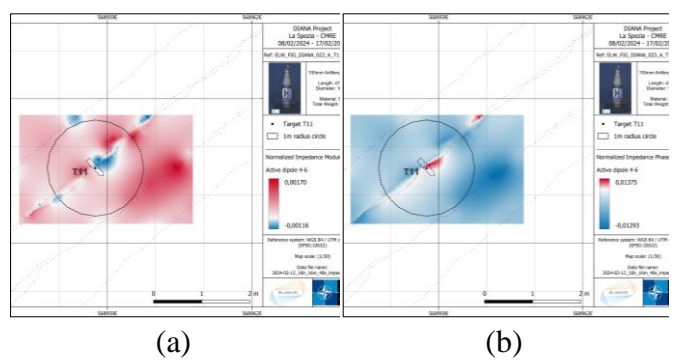


Figure 21: T11; Normalized impedance amplitude (a), phase (b)

VI. DISCUSSIONS

These tests have enabled us to identify key trends in the Octopulse sensor's detection performance based on four acquisition parameters:

- Frequency: for the same target with identical parameters, the 5kHz frequency provides better detection amplitude on one target, but poorer detection on all targets. A frequency of 1kHz provides a greater number of targets but a lower detection amplitude. Therefore, optimizing acquisition with a multi-frequency configuration is crucial. This can be achieved either by selecting a set of discrete frequencies or by emitting a multi-frequency signal.
- Dipole orientation: Relative dipole orientation (active or passive) to the target influences detection quality. Results show that better detection is obtained when the dipole is parallel to the longest dimension of the target. The 8 electrode Octopulse sensor creates numerous dipole orientations, maximizing the chances of target detection.

- Dipole length: Analysis on target T3 indicates that using longer dipoles tends to yield better detection.
 A dipole twice as long as another provided a detection amplitude significantly higher.
- Simultaneous acquisition of active and passive dipoles: Combining active and passive dipoles generally enhances detection quality compared to using only one type of dipole.

Additionally, the sign of the normalized impedance amplitude yields information about the electrical nature of the target: electrically insulating targets have positive values and electrically conductive targets have negative values. This is summarized in Table 3.

N°	Material	Active or Passive detection	Amplitude sign
T1	Plastic + Metal ballast	Passive	1
T2	Painted steel-sheet + rubber + cement	Active	+
T3	Metal	Passive	-
T4	Metal	Active	-
T5	Cement block	Active	+
Т6	Metal	Active	ı
T7	Metal	Active	ı
T8	Metal	Passive	-
Т9	Metal	Active	-
T10	Metal	Active	-
T11	Metal	Active	-

Table 3 Sign of normalized impedance amplitude versus target material.

VII. CONCLUSION

Mimicking the perception capability of weakly electric fish, a new impedance-based underwater sensing technology called CEDAR has been developed. This new principle has been incorporated into Elwave's Octopulse sensor. The impedance measurement uses both active and passive dipoles. The resulting amplitude and phase of the measurements can be plotted on 2D impedance maps to reveal underwater object locations and characterizations.

The Octopulse sensor was integrated on a ROV and tested at the NATO - CMRE centre. Sea trials data analysis demonstrated its ability to detect and characterize all conductive (ferromagnetic and non-magnetic) and insulating targets with high spatial resolution within the calibration zone.

ACKNOWLEDGEMENT

This work was supported by the NATO DIANA (Defence Innovation Accelerator for the North Atlantic) program, NATO-CMRE (Centre for Maritime Research and Experimentation). The CMRE test bed was sponsored by the U.S. Department of Defense Strategic Environmental Research and Development Program

(SERDP) and Environmental Security Technology Certification Program's (ESTCP) Munitions Response program.

REFERENCES

[LBLB17] S. Lanneau, F. Boyer, V. Lebastard and S. Bazille. Model based estimation of ellipsoidal object using artificial electric sense. The International Journal of Robotics Research, 2017.

[SLM07] J.R. Solberg, K.M. Lynch, and M.A. MacIver. Robotic electrolocation: Active underwater target localization. International Conference on Robotics and Automation, 2007.

[Gas06] E. Gasperikova, "Berkeley UXO discriminator (BUD) for UXO detection and discrimination," SERDP and ESTCP's Partners in Environmental Technology Technical Symposium & Workshop, Washington, DC, Nov. 28–30, 2006.

[Bar06] Barrowes, Benjamin "Handheld Frequency Domain Vector EMI Sensing for UXO Discrimination" SERDP MM1537 - FY06 Annual Report, The Strategic Environmental Research and Development Program (SERDP) 2006.

[McD06] Jim McDonald, "UXO Detection and Characterization in the Marine Environment" in proceedings Partners in Environmental Technology Technical Symposium & Workshop, Washington DC, November 2006.

[LM58] H.W. Lissmann and K.E. Machin. The mechanism of object location in gymnarchus niloticus and similar fish. The Journal of Experimental Biology, (35):451–486, 1958.

[CBG⁺98] A. Caputi, R. Budelli, K. Grant, and C. Bell. The electric image in weakly electric fish: Physical images of resistive objects in gnathonemus petersii. Journal of Experimental Biology, 201: pp. 2115–2128, 1998.

[ELW20] Q. Delplanque, L. Ifrek, F. Boyer, V. Lebastard. Detection method in electrically conductive media. Patent N° KR20230011308A. 2020